

# Investigation and Differentiation of Degradation Modes Affecting Series Resistance in Photovoltaic Cells and Modules

Roopmati Meena<sup>ID</sup>, Humaid Mohammed Niyaz, and Rajesh Gupta<sup>ID</sup>

**Abstract**—Degradation modes affecting series resistance ( $R_{\text{deg,modes}}$ ) are one of the major causes of performance degradation in outdoor operating photovoltaic (PV) modules. They have distinct loss incurring mechanisms under different climatic conditions. In this article, major  $R_{\text{deg,modes}}$  have been investigated for their impact on the electrical parameters and differentiated based on their distinct electrical signatures at both cell and module levels. For this purpose, the major  $R_{\text{deg,modes}}$  have been identified through cross-characterization of nine unaged PV modules subjected to temperature cycle, humidity freeze, and damp heat test conditions, using electroluminescence imaging and visual inspection. These  $R_{\text{deg,modes}}$  have been broadly categorized as metallization interruption, metallization corrosion, and cracks with loss in the active cell area. The spatial characteristics of various  $R_{\text{deg,modes}}$  have been modeled using distributed diode model of a solar cell, which has been experimentally validated. The change in fill factor has been chosen as a base metric to compare various  $R_{\text{deg,modes}}$ . The results show that combined case of metallization interruptions can be more severe than metallization corrosion. The maximum loss in power of up to 40% has been calculated for interruption at the finger-busbar interface. Furthermore, based on the loss incurring mechanism, various  $R_{\text{deg,modes}}$  exhibited distinct electrical signatures that were analyzed using normalized percentage change in voltage and current at the maximum power point, which has also been used to distinguish them. The distinct electrical signatures can be used for identification and nondestructive investigation of  $R_{\text{deg,modes}}$  in the PV modules under field-operating conditions.

**Index Terms**—Degradation modes affecting series resistance, distributed diode model (DDM), electroluminescence imaging, photovoltaic (PV) module, series resistance.

## I. INTRODUCTION

**D**EGRADATIONS under field-operating conditions affect the electrical parameters of a photovoltaic module, impacting its long-term reliability [1]. Herein, the current and series resistance ( $R_s$ ) of the PV module is affected by degradations concerning encapsulant and metallization components, respectively [2], [3]. Series resistance ( $R_s$ ) impacting degradations

has been the second most reported loss incurring mechanism “after encapsulant degradation” in photovoltaics modules under outdoor operating conditions [4], [5], [6]. In a crystalline-silicon (c-Si) technology based solar cell, the value of  $R_s$  in a cell depends on multiple components, which primarily include contact resistance, the sheet resistance of the emitter layer, finger resistance, busbar resistance, base resistance, and resistance of interconnecting ribbon. Degradation in one or more of these components leads to an increase in  $R_s$ , which can be attributed to different chemical, mechanical, and thermomechanical stress due to externalities, such as high moisture, high temperature, cyclic temperature variation, high wind speeds, hailstorms, under outdoor operating conditions [7]. The literature has extensively analyzed the effect of various  $R_s$  degradation on the reliability and long-term performance of solar cells and modules.

Kumar et al. [8] have performed the microstructural analysis of various moisture-ingression-induced degradation modes, affecting  $R_s$  through accelerated ageing of PV modules. The study has reported an increase in  $R_s$  of up to 13% primarily due to tin migration at the finger-wafer interface and the formation of silver oxide at cell cracks and edges. Furthermore, the authors have distinguished the degradation modes through their characteristic signature in dark lock-in thermography and electroluminescence (EL) images. Archana et al. [9] have investigated the impact of solder bond degradation at the cell interconnect in the field-aged PV modules. They have correlated high  $R_s$  regions with poorly soldered regions in the modules subjected to climatic conditions of Florida. Liu et al. [10] have qualitatively analyzed 30-year-old field-aged and warehouse-aged PV modules. The losses related to  $R_s$  degradation accounted for  $33\% \pm 1\%$ , with cell resistance losses amounting to 20% and interconnection-related losses amounting to 13%. Chattopadhyay et al. [11] have investigated 57 crystalline silicon modules under five different climatic conditions in India. The results show that a higher percentage of modules under hot and humid climatic conditions suffer from metallization corrosion compared to other zones. Bounouar et al. [12] have assessed the impact of an increase in the module operating temperature on the various component of  $R_s$  in the PV module. Herein, for a 6% power dissipation due to  $R_s$  in the module, the contribution of four components namely, finger resistance, busbar resistance, base resistance, and emitter resistance, is accounted for about 75%, 12%, 7%, and 3%, respectively. Asadpour et al. [13] have investigated the effect of finger thinning, finger delamination, and solder bond failure

Manuscript received 16 November 2022; accepted 19 January 2023. Date of publication 1 February 2023; date of current version 20 February 2023. (Corresponding author: Roopmati Meena.)

Roopmati Meena and Rajesh Gupta are with the Department of Energy Science and Engineering, Indian Institute of Technology Bombay, Mumbai 400076, India (e-mail: meenaroopmati@iitb.ac.in; rajeshgupta@iitb.ac.in).

Humaid Mohammed Niyaz is with the SmartHelio, New Delhi 110059, India (e-mail: humaidmohd4@gmail.com).

Color versions of one or more figures in this article are available at <https://doi.org/10.1109/JPHOTOV.2023.3239744>.

Digital Object Identifier 10.1109/JPHOTOV.2023.3239744

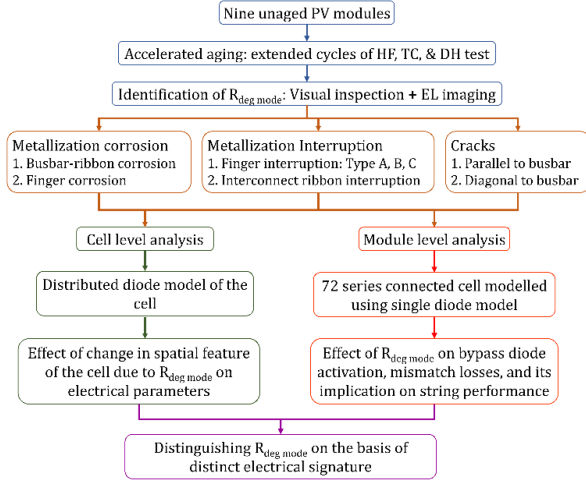


Fig. 1. Flow diagram of the methodology used in this work.

on the current–voltage ( $I$ – $V$ ) curve of the cells and module near short-circuit current ( $I_{sc}$ ) and open-circuit voltage ( $V_{oc}$ ) region. The study shows that aforementioned degradation modes can be misinterpreted as other degradation mode based on the changes in  $I$ – $V$  curves. Furthermore, thermomechanical stress degradations, such as breakage of fingers, interconnect ribbons, initiation, and propagation of cracks, have also been reported to affect  $R_s$  of the module [14], [15], [16].

The available literature on degradation modes affecting  $R_s$  ( $R_{deg,mode}$ ) can be broadly divided into two clusters; the first group has investigated the cumulative effect of various types of  $R_{deg,mode}$  on the electrical performance of the PV modules [17], [18], whereas the second group has focused on investigating the operating mechanism of  $R_{deg,mode}$  using several characterization techniques [19], [20], [21]. However, based on the spatial location of degradation, various  $R_{deg,mode}$  differ in their operating modes and loss-inducing mechanism, which can be crucial in determining their impact on the cell or module performance. In this work, the effect of the spatial location of  $R_{deg,mode}$  on the operating point of the cell and module has been analyzed to distinguish them based on their distinct electrical signatures at operating point. For this purpose, a distributed diode model (DDM) of a solar cell has been used to model spatial characteristics of various  $R_{deg,mode}$ . In addition, the effect of the nonuniform distribution of  $R_{deg,mode}$  at the module level has also been investigated.

The rest of this article is organized as follows. A detailed methodology has been given in Section II. The detailed results on the impact of various  $R_{deg,mode}$  on electrical parameters and their distinct signatures are given in Section III. Finally, Section IV concludes this article.

## II. METHODOLOGY

A systematic approach has been used to investigate and distinguish major  $R_{deg,mode}$  in PV cells and modules based on their distinct electrical signature. The schematic of the methodology adopted in this work is shown in Fig. 1.

$R_{deg,mode}$  have been induced in the nine unaged PV modules by subjecting them to extended cycles of accelerated ageing

TABLE I  
NUMERICAL VALUES OF THE ELECTRICAL PARAMETERS USED FOR THE SIMULATION OF SDM

Parameter	Value
$I_{sc}$ (A)	4.2
$I_0$ (A)	$6.5 \times 10^{-5}$
$n$	2.1
$R_s$ ( $\Omega$ )	0.01
$R_{sh}$ ( $\Omega$ )	36

tests namely, humidity freeze, damp heat, and thermal cycling tests, following the test procedure given in IEC 61215-2 standard [22]. Various  $R_{deg,mode}$  and their spatial characteristic patterns have been identified through pre- and posttest characterization of the PV modules using visual inspection and EL imaging technique. Based on the characterization results,  $R_{deg,mode}$  have been divided into three categories, viz. metallization corrosion, metallization interruption, and crack causing a loss in the active cell area. The identified spatial characteristics have been modeled in the DDM of a solar cell. The detailed information about DDM has been provided in the following section. Moreover, the impact of the nonuniform distribution of  $R_{deg,mode}$  at the module level has also been investigated. For this purpose, a PV module with 72 series-connected solar cells and three bypass diodes has been considered. These bypass diodes divide the PV module into three submodules, each with 24 cells and one bypass diode. The impact of degradation in  $R_s$  at the module level has been investigated using the single diode model (SDM) of the cell [23].  $R_s$  parameter for module-level analysis has been derived from cell-level analysis performed using DDM. The change from DDM to SDM has been made while considering the tradeoff between computational time and accuracy. The value of electrical parameters used for the simulation of SDM is given in Table I. Furthermore, the operating point parameters namely, the voltage at maximum power point ( $V_{max}$ ) and current at maximum power point ( $I_{max}$ ) of the cell and module have been analyzed to identify a distinct characteristic electrical signature of various  $R_{deg,mode}$ .

### A. DDM of Solar Cell

In this work, a DDM of a solar cell has been used to model the spatial characteristics of various  $R_{deg,mode}$ . For this purpose, the solar cell with three busbars has been divided into a grid of  $195 \times 390$  smaller subcells, where each subcell has been modeled as a combination of a current source ( $I_{sc}$ ), a diode, and a shunt resistance ( $R_{shunt}$ ), representing a p-n junction in a solar cell, as shown in Fig. 2.

Different subcells across the grid have been connected through different resistive components of a solar cell viz., sheet resistance, finger resistance, and busbar resistance, depending on the spatial position of the subcell. In this work, a half-cut cell with dimensions of  $15.6 \text{ cm} \times 7.8 \text{ cm}$  has been considered for DDM in the PSpice circuit simulator. However, the results and analysis presented in this work are also valid for other cell dimensions. The value for different components in a subcell,

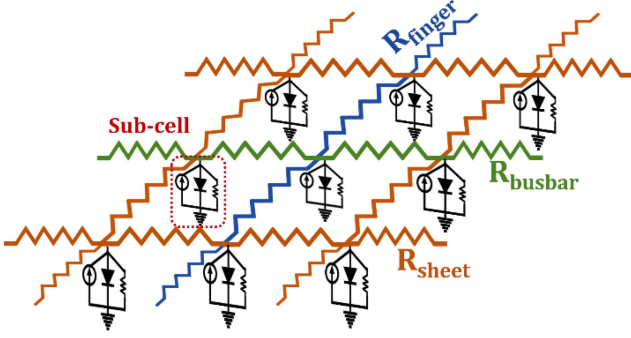


Fig. 2. Schematic showing DDM of the solar cell.

TABLE II  
PER UNIT NUMERICAL VALUES OF VARIOUS COMPONENTS USED IN DDM OF SOLAR CELL

Parameter	Value
$I_{sc}$ (A)	$6.87 \times 10^{-5}$
$I_o$ (A)	$8.6 \times 10^{-10}$
$n$	2.1
$R_{shunt}$ ( $\Omega$ /node)	$2.74 \times 10^6$
$R_{finger}$ ( $\Omega$ /cm)	$2.89 \times 10^{-4}$
$R_{busbar}$ ( $\Omega$ /cm)	$2.58 \times 10^{-5}$
$R_{sheet}$ ( $\Omega$ /sq.)	90

i.e.,  $I_{sc}$  (node), diode reverse saturation current ( $I_o$  (node)), and  $R_{shunt}$  (node), has been calculated from experimental  $I$ - $V$  curve data of solar cell using (1)–(3)

$$I_{sc} \text{ (node)} = \frac{I_{sc} \text{ (experiment)}}{\text{Number of active nodes in simulation circuit}} \quad (1)$$

$$I_o \text{ (node)} = \frac{I_o \text{ (experiment)}}{\text{Total number of nodes in the circuit}} \quad (2)$$

$$R_{shunt} \text{ (node)} = R_{shunt} \text{ (experiment)} \quad (3)$$

\* Total number of nodes in circuit.

In addition, the per unit value of different resistive components has also been obtained experimentally using the four-probe method, as described in [24]. The per unit values of different components used to model DDM are given in Table II. The DDM used in this work has been experimentally validated.

### B. Experimental Validation of DDM

The DDM has been experimentally validated by comparing the values of electrical parameters obtained from illuminated  $I$ - $V$  curve measurement of the solar cell with the parameters obtained through simulation using DDM. The  $I$ - $V$  curve obtained from the experiment and DDM simulation is shown in Fig. 3. The percentage error in different electrical parameters obtained from the DDM simulation with respect to values obtained through an illuminated  $I$ - $V$  curve is given in Table III. The percentage change in  $I_{sc}$  and  $V_{oc}$  is low. The negative change in maximum power point ( $P_{max}$ ), fill factor (FF), and  $R_s$  implies overestimation of these electrical parameters by DDM. It can be attributed

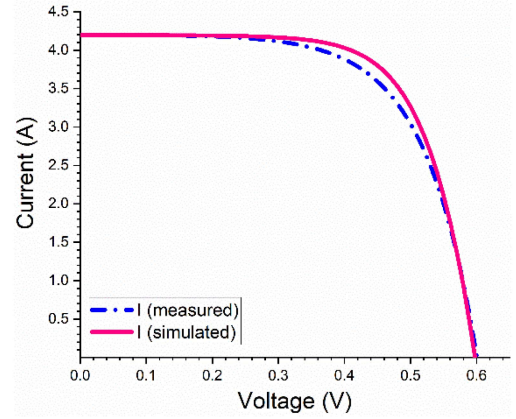
Fig. 3. Measured and simulated current–voltage ( $I$ - $V$ ) curve of the solar cell obtained from experiment and DDM, respectively.

TABLE III  
EXPERIMENTAL, SIMULATED, AND PERCENTAGE ERROR IN THE ELECTRICAL PARAMETERS USED FOR DDM OF SOLAR CELL

Electrical Parameters	Experimental value	Simulated value	Error (%)
Open-circuit voltage (V)	0.60	0.59	1.67
Short-circuit current (A)	4.20	4.20	0.00
Maximum power point (W)	1.62	1.72	-6.17
FF	64.11	69.18	-7.91

to the difference in the uniformity of electrical properties in a commercial solar cell and a simulated DDM circuit. A multicrystalline silicon solar cell contains multiple grain boundaries, which may act as loss incurring sites contributing to high  $R_s$ , thus resulting in high  $R_s$  in a commercial cell compared to DDM.

## III. RESULTS AND DISCUSSIONS

In this section, simulation results on different types of  $R_{deg, modes}$  have been discussed in detail. The EL images of PV modules subjected to extended accelerated tests have been used to identify the location and spatial characteristics of various  $R_{deg, modes}$ . For each degradation mode, the severity has been varied and its impact on electrical parameters has been analyzed. Herein, the change in FF has been selected as a base parameter to compare the severity of various  $R_{deg, modes}$  as it primarily gets influenced by parasitic resistances of cells, i.e.,  $R_s$  and  $R_{shunt}$ . Further effort has been made to distinguish the electrical signature of various  $R_{deg, modes}$  at the cell and module level.

### A. Spatial Characteristics of $R_{deg, modes}$

Based on visual inspection and analysis of EL images of the PV modules before and after accelerated ageing, various  $R_{deg, modes}$  were identified, which have been categorized under three categories viz., metallization interruption, metallization corrosion, and cracks causing a loss in the active cell area.



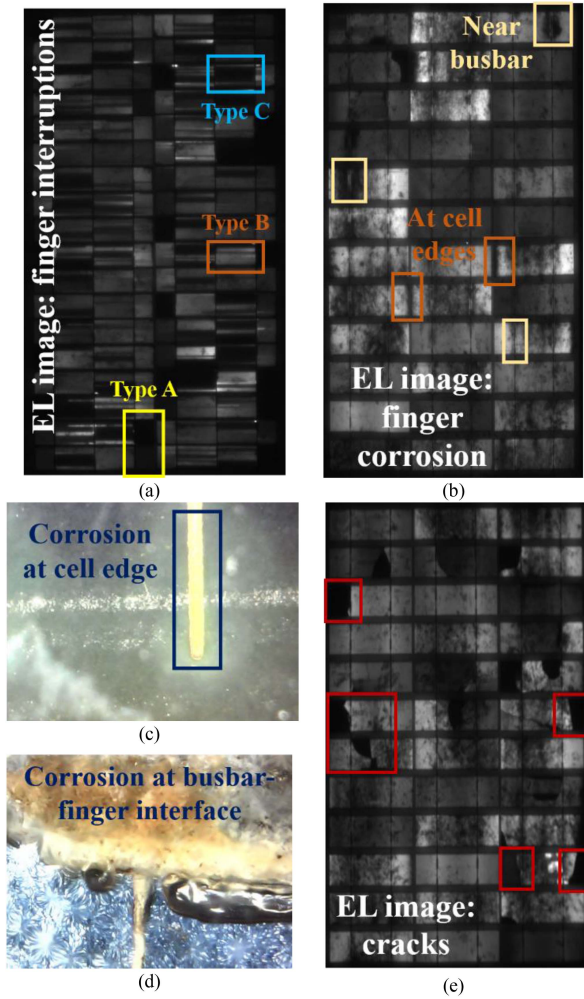


Fig. 4. (a) EL images of the module showing types of finger interruption. (b) EL image of module showing finger corrosion at the edges and around busbars, visual image showing (c) finger corrosion at cell edge, (d) corrosion at busbar-finger interface, and (e) EL image showing different crack orientations in solar cells.

The EL images showing spatial characteristics of different types of  $R_{deg, modes}$  are given in Fig. 4. Metallization interruption has been further subclassified into finger interruption and interconnect-ribbon interruption. Three prime locations of finger interruptions along the busbar-finger interface have been observed as outlined in Fig. 4(a).

Type A interruption has been defined as breakage in the finger at the single-point connection with the busbar. Type B interruption has been defined for the fingers located between busbars and interrupted at any one finger-busbar interface. Type C interruption has also been defined for the fingers located between the busbars but disconnected from both the finger-busbar interface. Similarly, two cases have been considered for interconnect ribbon interruption, i.e., breakage of one ribbon and simultaneous breakage of any two ribbons. Furthermore, metallization corrosion has been identified at multiple locations in the EL images, as shown in Fig. 4(b). Dark regions at the edges of solar cells and around busbar regions have been identified, which can be attributed to corrosion of fingers, corrosion of

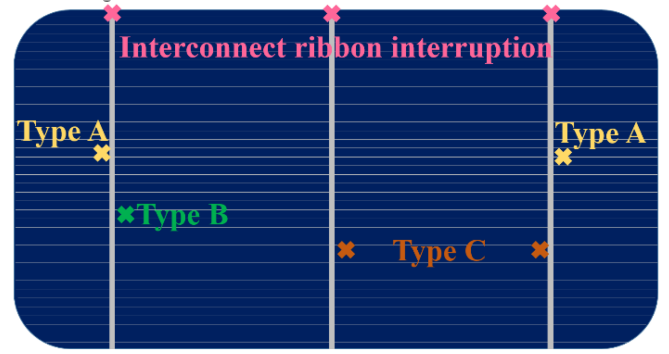


Fig. 5. Schematic showing different types of metallization interruptions.

busbars, and solder bond failure, as shown in Fig. 4(c) and (d). In this work, based on the spatial location of observed degradations, uniform corrosion over metallization has been considered for simulation purposes. Moreover, based on the analysis of EL images and the study of existing literature, two prominent crack orientations have been identified, as shown in Fig. 4(e). Cracks parallel to the busbar are the most frequently observed crack orientation as also visible in EL image, followed by cracks diagonal to busbar [25]. The spatial characteristics of the aforementioned  $R_{deg, modes}$  have been modeled in DDM and their impact on the electrical performance of solar cells and modules has been analyzed.

#### B. Analysis of $R_{deg, modes}$ on PV Cell Performance

In this section, the impact of  $R_{deg, modes}$  on the electrical parameters of the PV cell has been studied in detail. The percentage change in  $R_s$ ,  $P_{max}$ , and FF has been investigated with a change in the severity of the degradation modes. Furthermore, characteristic pattern in the operating point of the cell with a change in degradation severity has been analyzed to distinguish different  $R_{deg, modes}$ .

##### 1) Effect on Electrical Performance:

a) *Metallization interruption:* Metallization interruption has been classified into two types namely, finger interruption and interconnect ribbon interruption at cell edge. Schematic of the types of metallization interruptions simulated in this work is given in Fig. 5.

Successive fingers have been interrupted at the busbar-finger interface by removing the finger resistance component at the node corresponding to the busbar-finger interface in the DDM simulation circuit. The percentage loss in  $R_s$  and  $P_{max}$  for different types of finger interruption with the percentage change in FF is shown in Fig. 6. It can be observed that loss in  $P_{max}$  due to Type B interruption is negligible as the finger still has contact with a busbar from the noninterrupted end. While, for Type A interruption, the loss in  $P_{max}$  is proportional to the change in  $R_s$ .

However, for Type C interruption, with an increase in the number of interrupted fingers (severity of degradation), the slope of change in  $P_{max}$  is less than the change in  $R_s$ . The maximum loss in  $P_{max}$  up to 40% has been observed for the combined case of Type A+C finger interruption. A similar extent of loss

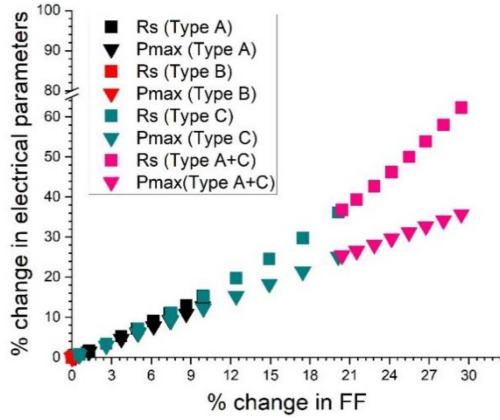


Fig. 6. Percentage change in series resistance and maximum power with change in FF for various types of finger interruptions.

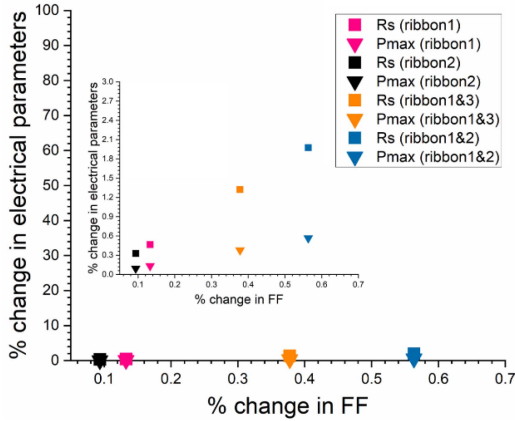


Fig. 7. Percentage change in series resistance and maximum power with change in FF for interconnect ribbon interruptions.

in  $P_{\max}$  has also been reported due to finger interruption caused by thermomechanical stress-induced  $R_s$  degradation [26], [27]. The corresponding increment in  $R_s$  for the combined case of type A+C interruption has been exponential. Furthermore, the maximum loss in FF has been around 30% for Type A+C interruption.

The percentage change in  $R_s$  and  $P_{\max}$  with change in FF due to interconnect ribbon interruption is given in Fig. 7. The maximum degradation in  $P_{\max}$  of 2% has been observed for the interruption of ribbons 1 and 2 together, which is very low compared to finger interruptions. It must be noted that for the cases of interruption in two ribbons, the impact of interruption in ribbons 1 and 2 on electrical parameters has been the same as due to interruption in ribbons 2 and 3. Hence, results pertaining to one of the aforementioned cases have been presented, i.e., interruption in ribbons 1 and 2.

The loss in the FF and  $P_{\max}$  due to metallization interruption can be understood based on the change in the current distribution and the drop in the voltage. In this regard, the change in FF can be perceived as the additional resistance that the current experience in the pathway to reach the external circuit in the presence of  $R_{\text{deg, modes}}$ . The interruption in the interconnect ribbon causes the current to cover a long path via fingers to reach the nearby ribbon connected to the external circuit. However, the drop in

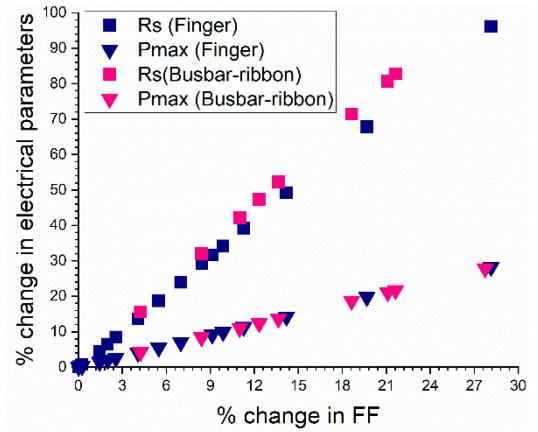


Fig. 8. Percentage change in series resistance and maximum power with change in FF for metallization corrosion.

voltage through finger resistance is low, resulting in a minor change in FF due to interconnect ribbon interruption. However, due to finger interruption, the low finger resistance component gets replaced by a high emitter/semiconductor resistance component at the interruption interface, leading to a high loss in FF due to the drop in the voltage with a cumulative increase in the number of interrupted fingers. Moreover, the current along the interrupted finger nodes is not collected leading to a high accumulative loss in  $P_{\max}$ .

*b) Metallization corrosion:* To model metallization corrosion, the resistance of the metal components viz., finger and busbar resistance has been systematically increased till the loss in FF has become similar to that obtained for metallization interruption, i.e., around 30%. The extent of loss in FF has been kept similar to compare the severity of the degradation modes concerning metallization components. The percentage loss in  $R_s$  and  $P_{\max}$  with change in FF due to metallization corrosion is shown in Fig. 8.

The increase in  $R_s$  due to corrosion primarily causes a drop in the voltage along the path of current flow. However, due to severe corrosion, the current collection also gets affected leading to a significant loss in  $P_{\max}$ . It must be noted that for a similar extent of loss in  $P_{\max}$ , the change in  $R_s$  due to busbar-ribbon corrosion is slightly more than finger corrosion. This can be because the busbar is the least resistant path in a solar cell, as a result, a high increase in busbar-ribbon resistance is needed to reach a similar extent of losses. Moreover, the comparison shows that loss in  $P_{\max}$  due to finger interruption is more than finger corrosion for a similar extent of loss in FF, implying that the former is a more severe degradation mode than the latter.

*c) Cracks:* In addition to metallization corrosion and interruption, cracks in the silicon wafers also affect the cell metallization network. In this work, the cracks causing a loss in the active cell area have been simulated. The schematic showing types of cracks simulated in this work is given in Fig. 9.

These crack orientations have been simulated in the DDM by removing the appropriate subcell nodes from the simulation circuit. Moreover, only cracks parallel to the busbar causing a loss in the active cell area have been considered, i.e., cracks to the left- or right-hand side of outer busbars 1 and 3. Based

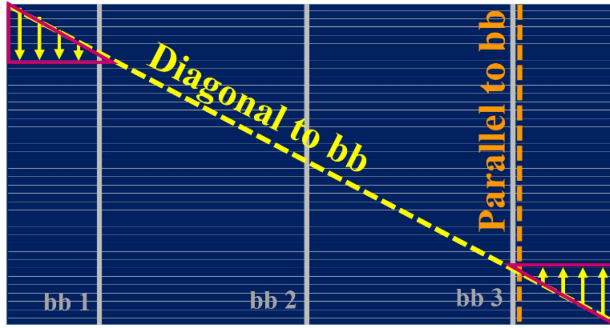


Fig. 9. Schematic showing different types of crack orientations simulated.

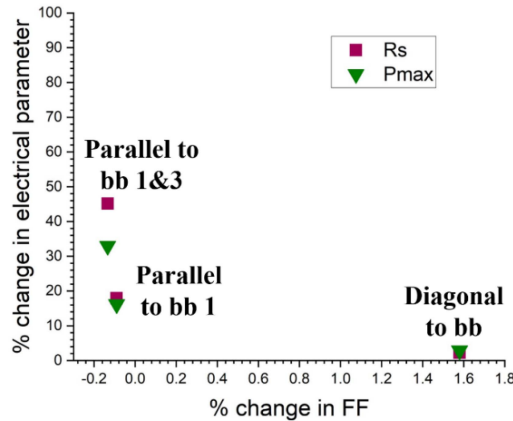


Fig. 10. Percentage change in series resistance and maximum power with change in FF for different types of crack orientations.

on the analysis of EL images [see Fig. 4(c)], a special case of two cracks in a single cell, parallel to the busbar has also been simulated. The loss in electrical parameters due to cracks of different orientations is given in Fig. 10. It can be observed that the maximum change in FF due to cracks is less than 2%. Whereas, loss in  $P_{\max}$  is proportional to the loss in the active cell area, which can be attributed to the loss in  $I_{sc}$ . Herein, the diagonal crack has shown the lowest loss in  $P_{\max}$  and the highest loss in FF amongst different crack orientations.

It can be understood based on the relation between crack orientation and the path that the current has to traverse to reach the external circuit in the presence of the diagonal crack. Due to the diagonal crack, the area of the cell between the crack and cell edge gets isolated from the busbar (marked by red triangles). As a result, the current has to traverse a longer, high resistance path through sheet resistance (marked by the yellow arrow in Fig. 9) to reach the external circuit, causing a loss in FF. While in the case of parallel cracks, the area between the crack and cell edges gets disconnected. However, there is no change in the path of current flow in the remaining intact region of the cell; thus, the change in FF for parallel cracks has been negligible. The increase in  $R_s$  for parallel cracks has been proportional to the loss in the active area, which can be attributed to the loss in the current ( $I$ ) ( $R_s = V/I$ ) for constant voltage ( $V$ ).

2) *Distinct Electrical Signature of  $R_{deg, modes}$* : In this section, different  $R_{deg, modes}$  have been simultaneously analyzed to identify their distinct electrical signature. For this purpose, the

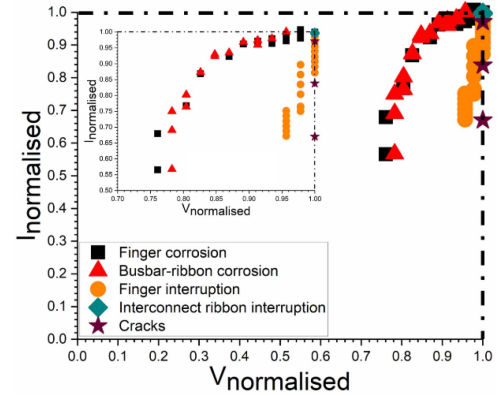


Fig. 11. Plot between  $I_{normalized}$  and  $V_{normalized}$  for a single cell corresponding to different  $R_{deg, modes}$ .

difference in the operating mechanisms of  $R_{deg, modes}$  has been studied in detail and their effect on the operating point of the cell has been investigated. The trend of percentage changes in  $I_{\max}$  and  $V_{\max}$  has been analyzed as normalized current ( $I_{normalized}$ ) and normalized voltage ( $V_{normalized}$ ); defined as the ratio of  $I_{\max}$  and  $V_{\max}$  in the presence of  $R_{deg, modes}$  to  $I_{\max}$  and  $V_{\max}$  of the cell in the absence of  $R_{deg, modes}$ , respectively. The plot between  $I_{normalized}$  and  $V_{normalized}$  for investigated  $R_{deg, modes}$  in a cell is given in Fig. 11. Based on the trend of change in normalized parameters, the graph has been divided into two regions, namely region-A and region-B.

$R_{deg, modes}$  in region-A have primarily caused a loss in  $I_{\max}$  of the cell, resulting in a vertical trend line in a normalized parameter graph. It includes cracks and metallization interruptions. The disruption in the metallization network caused by metallization interruption or cracks hampers the collection of current, leading to a loss in  $I_{\max}$ .  $R_{deg, modes}$  in the region-B include metallization corrosion, which has led to a loss in both  $I_{\max}$  and  $V_{\max}$  of the cell resulting in a diagonal trend line. The corroded metallization hinders the collection of generated current. Moreover, the flow of current through high resistance corroded metallization causes a drop in the voltage leading to a loss in  $V_{\max}$ . The extent of loss in  $I_{\max}$  is more for region-B degradation modes compared to region-A. The loss in  $I_{\max}$  due to the presence of  $R_{deg, modes}$  in the cells can lead to additional losses at a module level due to current mismatch, given that the degradation can have nonuniform distribution in the module under external operating conditions [28]. In this regard, the impact of nonuniform distribution of various  $R_{deg, modes}$  has also been analyzed on the module performance.

### C. Analysis of $R_{deg, modes}$ on PV Module Performance

This section analyses the impact of the nonuniform distribution of  $R_{deg, modes}$  at the module level. For this purpose, a PV module with 72 cells and three bypass diodes, each across a string of 24 cells has been simulated using the SDM of the solar cell. The degradation has been introduced in the 24 cells of a string and its impact on the power-voltage ( $P-V$ ) curve of the module has been analyzed with an increase in degradation severity. The maximum extent of degradation severity in a cell has been kept the same as in the DDM simulation. For this



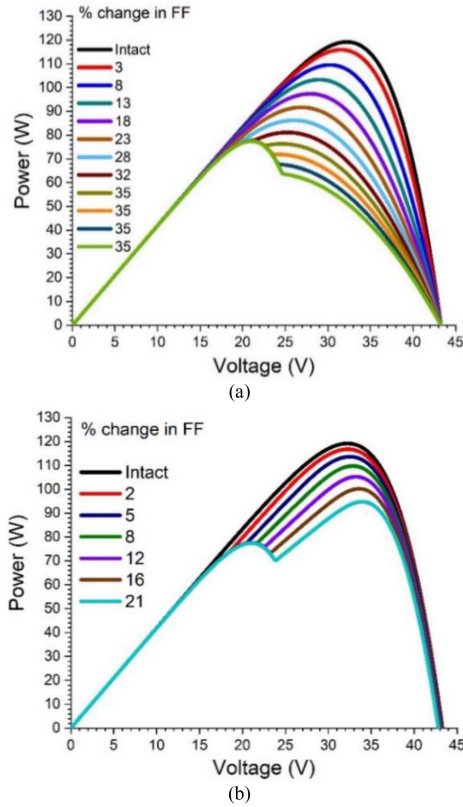


Fig. 12. Power-voltage ( $P$ - $V$ ) curves of the module with different extent of (a) metallization degradation and (b) cracked region in a string of the module.

purpose, the values of  $R_s$  in SDM corresponding to change in degradation severity have been calculated from the  $I$ - $V$  curve data obtained through the DDM of the cell. Moreover, the trend of  $I_{\text{normalized}}$  and  $V_{\text{normalized}}$  for the module has also been analyzed to distinguish  $R_{\text{deg,modes}}$  at the module level.

1) *Effect on Electrical Performance:* For module level analysis, metallization corrosion and interruption have been analyzed under the umbrella term of metallization degradation. The severity of degradation has been changed in the simulation by varying  $R_s$  of the cells in a string. The  $P$ - $V$  curves of the module for the varying extent of metallization degradation with change in FF are given in Fig. 12(a). The loss in FF has been high because of the additional mismatch loss in the cells of the module due to the nonuniform distribution of the degradation. Moreover, it can be observed that the change in FF has become constant with the activation of the bypass diode resulting in a constant global peak, characterized by the double peak in  $P$ - $V$  curves. It occurs as the equivalent resistance experienced by the current en route to the external circuit becomes constant with activation of the bypass diode.

Similarly, the impact of cracks on the module has also been studied by introducing the cracks in the string of 24 cells of the module. The  $P$ - $V$  curves for the varying extent of cracked areas are given in Fig. 12(b). Herein, the loss in the active area of up to 30% has been considered, which accounts for the simultaneous occurrence of two cracks parallel to the busbar. The loss in the active area has been simulated by systematically changing the value of  $I_{\text{sc}}$  in the SDM of cells. Herein, the reduction in global

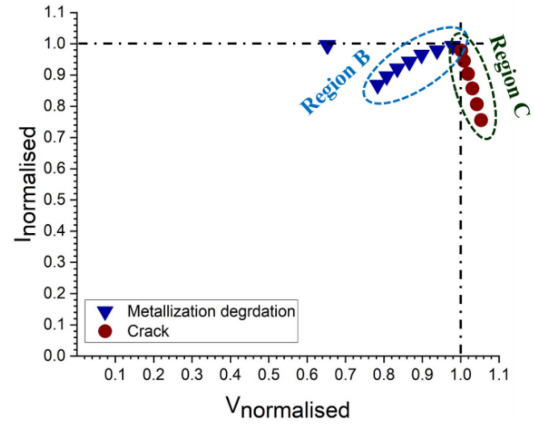


Fig. 13. Plot between  $I_{\text{normalized}}$  and  $V_{\text{normalized}}$  for a module corresponding to different  $R_{\text{deg,modes}}$ .

peak/maxima has led to a permanent loss in  $P_{\text{max}}$  of the module, which has induced a permanent mismatch loss in the module strings. It must be noted that for metallization degradation, the change FF has become constant with activation of the bypass diode; however, for cracks, the reduction in FF persists even after bypass diode activation for 30% loss in the active cell area.

2) *Distinct Electrical Signature of Series Resistance Affecting Degradation Modes:* The effect of the nonuniform distribution of  $R_{\text{deg,modes}}$  on  $I_{\text{max}}$  and  $V_{\text{max}}$  of the module has also been analyzed. The graph between  $I_{\text{normalized}}$  and  $V_{\text{normalized}}$  for metallization degradation and cracks in a string of the PV module is shown in Fig. 13. The metallization degradation, i.e., corrosion and interruption lead to losses in both  $I_{\text{max}}$  and  $V_{\text{max}}$  of the module, due to hindrance in the current collection and drop in voltage, respectively. However, with the activation of the bypass diode, the effect of mismatch in  $I_{\text{max}}$  gets eliminated. It has resulted in the shift of the diagonal trend toward the horizontal line. In the case of cracks, the trend in the shift of normalized parameters has been different than in a single cell. For a maximum of 30% loss in the active cell area, the loss in  $I_{\text{max}}$  has increased in proportion to the loss in the active area irrespective of activation of the bypass diode. Moreover,  $V_{\text{max}}$  of the module has increased. It can be attributed to the shift in the operating voltage of the cells in the string toward  $V_{\text{oc}}$  due to a reduction in string current, causing an overall increase in the module  $V_{\text{max}}$ . The effect of change in the operating point of the module due to  $R_{\text{deg,modes}}$  can affect the operation of the maximum power point tracking (MPPT) system in the PV plants. Wherein, it may cause the MPPT to operate at the local maxima of the modules leading to a reduction in output power.

#### IV. CONCLUSION

In this article, various degradation modes affecting series resistance ( $R_{\text{deg,modes}}$ ) have been investigated and differentiated based on their impact on the operating point of the PV cell and module. For this purpose, various types of  $R_{\text{deg,modes}}$  have been grouped into three categories namely, metallization corrosion, metallization interruption, and crack with loss in the active cell area. The cell level analysis shows a maximum loss in cell power ( $P_{\text{max}}$ ) of around 40% due to the interruption at

the finger-busbar interface for the fingers located between two busbars. The change in FF has been used as a base metric to compare various  $R_{\text{deg, modes}}$ . For a similar extent of loss in FF, the metallization interruptions are more severe than metallization corrosion in terms of loss in  $P_{\text{max}}$ . Furthermore, the analysis of the operating points showed distinct electrical signatures for different  $R_{\text{deg, modes}}$ . The metallization corrosion affected both current ( $I_{\text{max}}$ ) and voltage ( $V_{\text{max}}$ ) at the maximum power point, whereas the cracks only impacted  $V_{\text{max}}$ . On the other hand, the metallization interruption mainly affected  $I_{\text{max}}$ .  $R_{\text{deg, modes}}$  impacting  $I_{\text{max}}$  of the cell will lead to the current mismatch and formation of hotspots with and without shading at the module level.

At the module level, with the activation of the bypass diode, metallization corrosion and interruptions caused a loss in  $V_{\text{max}}$  of the module. However, the cracks led to a decrement of  $I_{\text{max}}$  with an increase in  $V_{\text{max}}$  of the module due to a shift in the operating point of cells in the string. This change in the operating point of the module due to  $R_{\text{deg, modes}}$  can affect the operation of MPPT devices. The distinct effect of various  $R_{\text{deg, modes}}$  on the operating point of cell and module can be utilized for nondestructive investigation of these degradation modes under outdoor operating conditions. In order to extend this study for field application, the systematic data analysis of electrical parameters needs to be structured. In future, the module level study would be extended to string level with the aim to capture early signature of  $R_s$  degradation.

#### ACKNOWLEDGMENT

The authors would like to thank Dr. Sudhanshu Mallick and Mr. Purnendu Kartikay from Particulate Materials Lab, IIT Bombay, Mumbai, India, for providing access to their laboratory for conducting four-probe measurements.

#### REFERENCES

- [1] M. M. Fouad, L. A. Shihata, and E. S. I. Morgan, "An integrated review of factors influencing the performance of photovoltaic panels," *Renew. Sustain. Energy Rev.*, vol. 80, pp. 1499–1511, May 2017, doi: [10.1016/j.rser.2017.05.141](#).
- [2] V. E. Puranik, R. Kumar, and R. Gupta, "Generalized quantitative electroluminescence method for the performance evaluation of defective and unevenly degraded crystalline silicon photovoltaic module," *Prog. Photovolt. Res. Appl.*, pp. 1–14, May 2022, doi: [10.1002/pip.3632](#).
- [3] R. Meena, M. Kumar, S. Kumar, and R. Gupta, "Comparative degradation analysis of accelerated-aged and field-aged crystalline silicon photovoltaic modules under tropical climatic conditions," *Results Eng.*, vol. 16, Jul. 2022, Art. no. 100674, doi: [10.1016/j.rineng.2022.100674](#).
- [4] S. Chattopadhyay et al., "Visual degradation in field-aged crystalline silicon PV modules in India and correlation with electrical degradation," *IEEE J. Photovolt.*, vol. 4, no. 6, pp. 1470–1476, Nov. 2014, doi: [10.1109/JPHOTOV.2014.2356717](#).
- [5] C. Peike et al., "Origin of damp-heat induced cell degradation," *Sol. Energy Mater. Sol. Cells*, vol. 116, pp. 49–54, 2013, doi: [10.1016/j.solmat.2013.03.022](#).
- [6] J. M. Kuitche, R. Pan, and G. Tamizhmani, "Investigation of dominant failure mode(s) for field-aged crystalline silicon PV modules under desert climatic conditions," *IEEE J. Photovolt.*, vol. 4, no. 3, pp. 814–826, May 2014, doi: [10.1109/JPHOTOV.2014.2308720](#).
- [7] B. Bora et al., "Failure mode analysis of PV modules in different climatic conditions," *IEEE J. Photovolt.*, vol. 11, no. 2, pp. 453–460, Mar. 2021, doi: [10.1109/JPHOTOV.2020.3043847](#).
- [8] S. Kumar, R. Meena, and R. Gupta, "Imaging and micro-structural characterization of moisture induced degradation in crystalline silicon photovoltaic modules," *Sol. Energy*, vol. 194, pp. 903–912, 2019, doi: [10.1016/j.solener.2019.11.037](#).
- [9] A. Sinha et al., "Solder bond degradation of fielded PV modules: Correlation between performance, series resistance and electroluminescence imaging," in *Proc. IEEE Conf. Rec. Photovolt. Spec. Conf.*, 2019, pp. 2566–2570, doi: [10.1109/PVSC40753.2019.8980678](#).
- [10] Z. Liu et al., "Quantitative analysis of degradation mechanisms in 30-year-old PV modules," *Sol. Energy Mater. Sol. Cells*, vol. 200, 2019, Art. no. 110019, doi: [10.1016/j.solmat.2019.110019](#).
- [11] S. Chattopadhyay et al., "Correlating infrared thermography with electrical degradation of PV modules inspected in all-India survey of photovoltaic module reliability 2016," *IEEE J. Photovolt.*, vol. 8, no. 6, pp. 1800–1808, Nov. 2018, doi: [10.1109/JPHOTOV.2018.2859780](#).
- [12] S. Bounouar et al., "Assessment of series resistance components of a solar PV module depending on its temperature under real operating conditions," *Int. J. Renew. Energy Res.*, vol. 10, no. 4, pp. 1555–1565, 2020, doi: [10.20508/ijrer.v10i4.11240.g8040](#).
- [13] R. Asadpour, X. Sun, and M. A. Alam, "Electrical signatures of corrosion and solder bond failure in c-Si solar cells and modules," *IEEE J. Photovolt.*, vol. 9, no. 3, pp. 759–767, May 2019, doi: [10.1109/JPHOTOV.2019.2896898](#).
- [14] A. Morlier, F. Haase, and M. Kontges, "Impact of cracks in multicrystalline silicon solar cells on PV module power—A simulation study based on field data," *IEEE J. Photovolt.*, vol. 5, no. 6, pp. 1735–1741, Nov. 2015, doi: [10.1109/JPHOTOV.2015.2471076](#).
- [15] H. Mohammed Niyaz, R. Meena, and R. Gupta, "Impact of cracks on crystalline silicon photovoltaic modules temperature distribution," *Sol. Energy*, vol. 225, pp. 148–161, 2021, doi: [10.1016/j.solener.2021.07.038](#).
- [16] S. Kumar and R. Gupta, "Investigation and analysis of thermo-mechanical degradation of fingers in a photovoltaic module under thermal cyclic stress conditions," *Sol. Energy*, vol. 174, pp. 1044–1052, 2018, doi: [10.1016/j.solener.2018.10.009](#).
- [17] J. D. Bastidas-Rodriguez, E. Franco, G. Petrone, C. A. Ramos-Paja, and G. Spagnuolo, "Model-based degradation analysis of photovoltaic modules through series resistance estimation," *IEEE Trans. Ind. Electron.*, vol. 62, no. 11, pp. 7256–7265, Nov. 2015, doi: [10.1109/TIE.2015.2459380](#).
- [18] E. E. van Dyk and E. L. Meyer, "Analysis of the effect of parasitic resistances on the performance of photovoltaic modules," *Renew. Energy*, vol. 29, no. 3, pp. 333–344, 2004, doi: [10.1016/S0960-1481\(03\)00250-7](#).
- [19] S. Kumar, R. Meena, and R. Gupta, "Finger and interconnect degradations in crystalline silicon photovoltaic modules: A review," *Sol. Energy Mater. Sol. Cells*, vol. 230, 2021, Art. no. 111296, doi: [10.1016/j.solmat.2021.111296](#).
- [20] P. Hülsmann and K.-A. A. Weiss, "Simulation of water ingress into PV-modules: IEC-testing versus outdoor exposure," *Sol. Energy*, vol. 115, pp. 347–353, 2015, doi: [10.1016/j.solener.2015.03.007](#).
- [21] J.-H. Kim, D. Kim, and N. Park, "Study on mitigation method of solder corrosion for crystalline silicon photovoltaic modules," *Int. J. Photoenergy*, vol. 2014, 2014, Art. no. 809075, doi: [10.1155/2014/809075](#).
- [22] *Terrestrial Photovoltaic (PV) Modules - Design Qualification and Type Approval - Part 2: Test Procedures*, IEC 61215-2: 2021, International Electrotechnical Commission, London, U.K., 2021.
- [23] M. Azzouzi, D. Popescu, and M. Bouchahdane, "Modeling of electrical characteristics of photovoltaic cell considering single-diode model," *J. Clean Energy Technol.*, vol. 4, no. 6, pp. 414–420, 2016, doi: [10.18178/jocet.2016.4.6.323](#).
- [24] D. L. Meier et al., "Determining components of series resistance from measurements on a finished cell," in *Proc. IEEE Conf. Rec. 4th World Conf. Photovolt. Energy Convers.*, 2007, pp. 1315–1318, doi: [10.1109/WCPEC.2006.2796566](#).
- [25] M. Köntges, S. Kajari-Schröder, and I. Kunze, "Crack statistic for wafer-based silicon solar cell modules in the field measured by UV fluorescence," *IEEE J. Photovolt.*, vol. 3, no. 1, pp. 95–101, Jan. 2013, doi: [10.1109/JPHOTOV.2012.2208941](#).
- [26] S. Roy, S. Kumar, and R. Gupta, "Investigation and analysis of finger breakages in commercial crystalline silicon photovoltaic modules under standard thermal cycling test," *Eng. Failure Anal.*, vol. 101, pp. 309–319, 2019, doi: [10.1016/j.engfailanal.2019.03.031](#).
- [27] S. Kumar, S. Roy, and R. Gupta, "Characterization of degradation under standard environmental testing methods for crystalline silicon photovoltaic modules," *Int. J. Power Energy Res.*, vol. 1, no. 3, pp. 150–158, 2017, doi: [10.22606/ijper.2017.13002](#).
- [28] R. Meena, M. Kumar, and R. Gupta, "Investigation of dominant degradation mode in field-aged photovoltaic modules using novel differential current-voltage analysis approach," *Prog. Photovolt. Res. Appl.*, vol. 30, pp. 1312–1324, 2022, doi: [10.1002/pip.3580](#).